Compressive behaviour of carbon fibres micropillars by in situ SEM nanocompression

T.S. Guruprasad, Vincent Keryvin, Guillaume Kermouche, Yvan Marthouret, Sergio Sao Joao

Compressive behaviour of carbon fibres micropillars by in situ SEM nanocompression

T. S. Guruprasad[a,b], V. Keryvin[a,*], G. Kermouche[c], Y. Marthouret[c], S. Sao-Joao[c]

[a] *Univ. Bretagne Sud, UMR CNRS 6027, IRDL, F-56100 Lorient, France*
[b] *Department of Mechanical and Manufacturing Engineering, Manipal Institute of Technology, Manipal Academy of Higher Education, Manipal, 576104, India*
[c] *Mines Saint-Etienne, CNRS, UMR 5307 LGF, Centre SMS, F – 42023 Saint-Etienne, France*

Abstract

As carbon fibres are heterogeneous, anisotropic and small in size, the determination of their mechanical properties is rather difficult. Here, the compressive behaviour of two different carbon fibres is studied using in situ compression tests on micro-pillars with scanning electron microscopy (SEM). The mode of failure is axial splitting. Large hysteretic loops are observed, associated with crack development, but no or small permanent deformation is visible. The compressive properties (modulus, strength) of these pillars are lower than the tensile properties of the fibres (128 GPa and 2.38 for UTS50 respectively and 110 GPa and 2.36 GPa for HR40 respectively). The mechanisms involved are studied and compared with those of various other experimental techniques. The core-shell structure of the fibres is at the origin of these inferior properties (the pillar is associated with the core). The nano-buckling scenario of crystalline carbon stacks constrained by the shear stiffness of the fibre is in agreement with our moduli and strength results.

Keywords: Carbon fibres; Microcompression; Micropillars; Nanobuckling; Compressive strength; Compression modulus

*Corresponding author: vincent.keryvin@univ-ubs.fr (Vincent Keryvin)

1. Introduction

Carbon fibres are widely used in continuous fibre composites. For example, embedded in a polymer matrix, carbon fibre reinforced polymer (CFRP) composites are employed for their excellent specific mechanical properties. In general, the mechanical properties of CFRP in compression are relatively lower than in tension, which limits their use in some applications. To improve these mechanical properties, it is important to understand the deformation mechanisms in compression of both composites and carbon fibres since for fibres crushing failure mechanisms may be at stake.

The diameters of carbon fibres are small and lower than $10\ \mu\mathrm{m}$ which makes it difficult to determine straightforwardly compressive properties from experiments. In literature, different experimental techniques were used to determine their compressive strength, namely elastic loop test [1], fibre recoil method [2], direct fibre compression [3–6], two points bending [7], four points bending [8]. All these techniques, though, have some limitations including the lack of precise instrumentation, crude assumptions in data analysis or the difficulty to avoid the buckling of the fibre. Usually, strength values are lower than the tensile strength ones, and the range of reported values in terms of a ratio compressive to tensile strengths is very large, namely 30-110% depending on the type of carbon fibre tested and the test itself. In addition, there exists no convergence of experimental results in terms of compressive strength values for a given fibre type [9]. For example, on the standard modulus T300 carbon fibre, contrasting values of 1.8 GPa [4] and 3.7 GPa [6] were reported. In recent years, a promising technique for determining the mechanical properties of micron sized samples in compression has been proposed in the form of micro-pillar compression testing. The advantage of such a test is that the stress state is uniaxial and quasi-homogeneous. This technique has been widely used to determine the compressive properties of various materials such as metals [10], polymers [11], amorphous materials [12], nano-laminates [13, 14]. Very recently, Wang et al. [15], Herráez et al. [16] carried out such experiments on carbon fibres. One

objective of this study is to bring additional results on different carbon fibres with the use of micro-pillar compression testing to this very limited literature database.

The combined use of scanning electron microscopy (SEM) and mechanical testing has become very popular these last 20 years [12]. A second objective of this work is therefore to perform in situ SEM micro-pillar compression testing to closely relate deformation and failure mechanisms to the mechanical response of the test namely the stress-strain curve. In doing so we will also use advantageously cyclic tests.

Carbon fibres are strongly anisotropic and they exhibit very different mechanical properties in longitudinal and transverse directions; for instance, elastic moduli differ usually by more than 20. These considerable differences come from the manufacturing process (especially the maximum temperature reached during synthesis) that impacts the internal structure of fibres, which is indeed heterogeneous.

The compressive strength has been reported as being dependent on micro-structural components such as the size of unit graphite crystals, the orientation parameter of the carbon layer stacks [4], the axial length and orientation of the micro-voids [3, 5] ... (See a recent review on this topic [17].) The mechanisms at stake during compression of carbon fibres are nevertheless still not fully understood. The last objective of this paper is thus to discuss our experimental results at the light of these proposed mechanisms and estimations.

The study is organised as follows. Micro-pillars of two PAN based carbon fibres having different elastic tensile moduli are fabricated using focused ion beam technique. They are compressed in situ inside a SEM chambre with a nano-indenter device having a flat punch diamond indenter. Both static tests and cyclic tests are performed in the displacement control mode and raw data from experiments are analysed. The possible experimental artefacts are carefully investigated. Then, the compression strength and mechanism of failure of two carbon fibres are discussed.

2. Materials and methods

2.1. Materials

Two different commercially available PAN (polyacrylonitrile) based carbon fibres were chosen for investigation. The first one is UTS50 (Teijin), which is a standard modulus (SM) type, and the second one is HR40 (Mitsubishi), which is a high modulus (HM) type. The fibres were part of cured composite pre-pregs, with an epoxy matrix (Gurit Se84 LV) and a fibre volume fraction of around 55%, used in other studies [18, 19]. (The cure was made at 120^{o}C under 7 bar.) The diameter of UTS50 carbon fibre was 7 μm, and that of HR40 was 6 μm. Their longitudinal moduli were 240 GPa (UTS50), and 375 GPa (HR40) known from their data sheets [20, 21].

2.2. Specimen preparation

Samples with 1×1 cm^2 size and a thickness of 0.5 cm were cut from the carbon fibre composites using a diamond disc cutter such that the axis of the fibres was in the thickness direction (longitudinal direction). The surface of the sample was polished with silicon carbide papers of 1000, 2000, and 4000 grit and then with diamond suspensions having particle sizes of 3 μm and 1 μm and finally, with colloidal silica of particle size of 0.03 μm. The micro-pillars were then machined by Focus Ion Beam (FIB) machining using a Thermo Scientific Helios NanoLab DualBeam microscope. Initially, the basic pillar shapes were prepared using high currents (30 kV, 2.5 A), then, smaller currents (30 kV, 80 pA) were used to refine the geometry to obtain the desired size. The micro-pillars had diameters ~ 3.5 μm and height ~ 8.5 μm so that the aspect ratio of pillar height to diameter of $\sim 2:1$ was maintained to avoid buckling during the deformation. In order to avoid material re-deposition, all the pillars were produced by annular machining process from the outside to the inside so that the pillar was globally coaxial to the fibre. The pillars height, top, and bottom diameters were measured using a scanning electron microscope (SEM). The taper angles of the UTS50 and HR40 micro-pillars were found to be 2°.

2.3. Micro-pillar compression tests

The micro-compression tests on the micro-pillars were performed using an ALEMNIS in situ nano-indenter apparatus in a Zeiss Gemini supra 55VP SEM. The nano-indenter apparatus was fitted with a diamond flat punch indenter of diameter $10\ \mu\mathrm{m}$ to test the micro-pillars. Further details of this in situ nano-indenter apparatus are given in Kermouche et al. [12]. The compression tests were conducted in the displacement controlled mode with a displacement rate of 50 nm/s, such that a constant strain rate of $\sim 6 \times 10^{-4}\mathrm{s}^{-1}$ was kept for all the tests. The force (F) versus displacement curves were recorded during the compression tests. The micro-pillars were tested with both continuous and cyclic loading conditions. Two samples were used for each type of fibre and for each type of loading. For cyclic tests, the loadings were applied such that the displacement is gradually increased from linear elastic regime to 30% of its fracture strain (breakage). Pillars were compressed with repeated loading and unloading by increasing the displacement at every next cycle. At each cycle, the displacement was increased by 100 nm up to 1000 nm with some cycles only in the elastic regime.

The measured displacements (u_{mes}) from the micro-compression tests were corrected (see details elsewhere [12]) by subtracting the displacements due to both frame stiffness (K_f) and the substrate stiffness (K_s), using the following relation (u_{pil} is the corrected displacement).

$$u_{pil} = u_{mes} - \frac{F}{K_{eff}},\ K_{eff} = \left[\frac{1}{K_f} + \frac{1}{K_s}\right]^{-1} \tag{1}$$

The frame stiffness, $K_f = 0.25$ mN/nm was determined from calibration using silica (a-SiO_2) micro-pillar samples [12]. The substrate beneath the pillar may deform when pillar undergoes deformation due to applied load, in which the base of the pillar penetrates into the substrate. The substrate deformation can be approximated by following Sneddon's

equation [22] in terms of substrate stiffness, which is given by,

$$K_s = 2\, M_s\, r_{bot} \tag{2}$$

where M_s is the indentation modulus of the substrate and r_{bot} is the radius of the bottom of the micro-pillar. For isotropic materials, $M_s = \frac{E}{1-\nu^2}$, where E and ν are Young's modulus and Poisson's ratio, respectively. For anisotropic materials, such as carbon fibres, the indentation modulus of the material can be determined from nanoindentation tests. In our case, values were taken from a previous study [23]. The engineering stress-strain curves were determined from the load versus displacement curves using initial length and initial cross-sectional area of the micro-pillar. The initial cross-sectional area was taken at half height of the micro-pillar. The true stress-strain curves were determined based on radial expansion of the pillar with a constant Poisson's ratio of 0.3. This crude approximation has no influence on the results of this work.

3. Results

3.1. Mechanical response of the micro-compression test

The representative force–displacement plots of UTS50 carbon fibres are shown in Figure 1, where the fibres are tested until complete failure. The last part of the curve (above $\sim$ 2000 nm) is meaningless since the samples are already broken and reloaded. This figure shows the reproducibility of the test. Figure 2 shows the engineering stress-strain response of UTS50 carbon fibres and the corresponding SEM images at different stages of strain. (Associated videos for both fibres are found in Supplementary A.) The first stage is a linear regime (from point A), where the pillar undergoes nearly homogeneous deformation (see Supplementary B for a Finite Element Analysis). With the increase of compressive strain, the slope suddenly starts to decrease. A maximum of the stress is then reached (point B). We will refer, *arbitrarily*, to this inflection point as the onset of pseudo-yielding. Indeed, as seen hereafter there is no plasticity at stake. At

this inflection point, the pillar begins to fracture by axial splitting (marked by an ellipse) initiating at or close to the contact surface by formation of crack(s). This is in complete agreement with the recent results of Wang et al. [15]. Pseudo-yielding is therefore associated to the onset of axial splitting and not to some mechanisms found in metallic alloys such as dislocations glide or in polymers such as molecular chains movement. With further increase of strain, other cracks appear and already existing cracks propagate (see point C) while the stress sightly decreases. Point D corresponds to a sudden and dramatic decrease in stress (force, see Fig. 1). The corresponding image confirms that the failure of the specimen is by extensive axial splitting. From C to D the stress slightly increases. Actually, converting the engineering stress to true stress (see later in Fig. 4) shows that it is a quasi-plateau between points C and D. There is no hardening-like behaviour. This is the only motivation of plotting the true stress - true strain curves. This plateau-like behaviour is very similar to that of some polymers in compression (see for instance Ref. [24] on an amorphous thermoplastics or Ref. [12] on amorphous silica in micro-pillar compression).

Figure 3 shows the engineering stress-strain response of UTS 50 micro-pillars submitted to cyclic compressive loads, and the corresponding SEM images at four different locations marked on the curves. Four cycles of loading and unloading curves are shown. The first two cycles were chosen in the linear regime (before point B in Fig. 2). In this regime, the loading and unloading curves are nearly the same. The behaviour is fully reversible and therefore referred to as linear elastic. This is a new result as compared to Wang et al. [15] who performed their cyclic tests at loads too high to stay in this linear regime. The third and fourth cycles were chosen to be after the linear regime (after point B in Fig. 2). The third cycle has a maximum applied strain indicated as point B before unloading. We can notice a crack opening in the corresponding SEM image (marked by an ellipse). In this case, the behaviour is again reversible in the mechanical sense, in the way that there is no irreversible strain after unloading. Yet, it is not fully reversible, in a thermodynamic sense, since loading and unloading curves are not the same; some

energy has been dissipated. The fourth cycle has a maximum applied strain indicated as point C before unloading. We can notice in the corresponding SEM image an increase of the number of cracks and their lengths with respect to image B. This is in complete agreement with the recent results of Wang et al. [15]. After unloading (point D), the same reversibility mentioned above is noticed. Let us note that at the beginning of a new cycle the starting displacement is shifted slightly to the right, possibly due to some very small drift in the sensors of the nano-indenter apparatus. We can notice in the corresponding SEM image that cracks are no longer visible so that the pillar looks pristine. We can conclude that there is no plasticity (existence of permanent deformation) during micro-compression of these carbon fibres. From the results, it can even be concluded that the irreversible behaviour is only linked to the formation and growth of cracks with the axial splitting mechanism.

Figure 4 compares the mechanical behaviour of both carbon fibres micropillars from micro-compression tests. UTS50 and HR40 fibres are compressed up to complete failure, the post-failure data points being removed. The behaviour is the same for both fibres. A more precise description for HR40 is found in the Supplemental C.

3.2. Compression modulus

Figure 5 shows an example of the determination of a compressive elastic modulus, E_c^p, of a UTS50 carbon fibre micropillar. We chose to take a relatively wide range of strains ($\sim$ 0.5 %) in order to have enough data points for our linear fit to be meaningful. Table 1 shows the results obtained for both fibres. Note that the value of the compressive modulus is highly dependent on the value of the indentation modulus of the carbon fibre used to calibrate the compliance of the test and in particular the stiffness of its substrate M_s. For M_s = 80 GPa (taken from Ref. [23]) we have E_c^p = 128 $\pm$ 5 GPa for UTS50. For M_s = 70 GPa [23], we have E_c^p = 110 $\pm$ 12 GPa for HR40 (cf. Table 1). For M_s = 50 GPa (arbitrary value taken for comparison) we have E_c^p = 210 $\pm$ 12 GPa for UTS50 and 135 $\pm$ 29 GPa for HR40. The values reported in Table 1 are particularly low compared

to the tensile modulus of carbon fibres (see Table 1) and are in fact quite similar when comparing the two fibres, as visually shown in Fig. 4.

3.3. Definition of a compressive strength

For both UTS50 and HR40 carbon fibres, we observed a clear inflection point which is approximately at $\sim 3\%$ strain. At this point, there is clear evidence of the presence of a crack, and a 1% offset line drawn from the linear part of curve intersects this inflection point. The method of determining the inflection point is shown from engineering stress versus strain response of UTS50 carbon fibres in Fig. 6. The inflection point is nearly seen at an offset line at $\approx 1\%$ strain, and that point is taken as the compressive strength. We observed similar inflection point for HR40 carbon fibres. It is to be noted that this corresponds for both fibres to the beginning of the plateau. Let us highlight that this corresponds to the onset of splitting observed by SEM. The values of compressive strength (X_c^f) obtained from tests for both carbon fibres are given in Table 2.

Herráez et al. [16] studied on AS4 SM carbon fibre and used a 2% offset in displacement for determining the compressive strength since there was no clear point of inflection. Wang et al. [15] took the maximum stress reach for defining the compressive strength. We could have also used, which is made classically for metals, a definition with a 0.2 % offset. This does not change dramatically our results.

4. Discussion

4.1. Compression modulus of the pillar versus that of the fibre

The compressive moduli obtained in this study are clearly very low compared to reported tensile moduli of carbon fibres. Besides, they are very comparable for SM (UTS50) and HM (HR40) fibres while their tensile moduli are very different (240 vs 375 GPa). We investigate in this section this potential issue. In the two studies we found in the literature on microcompression of carbon fibre pillars [15, 16], only one reported moduli values. Indeed, Wang et al. [15] found on SM, IM and HM fibres the

same value of 60 GPa, therefore much lower again than the tensile moduli of fibres. It is known that the microcompression test on pillars is not designed for precise elastic stiffness measurement. Nonetheless, such a huge difference is not expected. Besides, the two carbon fibres exhibit the same compressive modulus. Therefore, we wondered whether this might come from a difference in structure and thus in properties of pillars and fibres. It is known that there is a skin (or shell) / core structure in carbon fibres [25]. The structure is different between the shell and the core, hence different mechanical properties are at stake. Kobayashi et al. [26] analysed their Raman spectroscopy and X-ray diffraction results to indicate that the skin modulus of a HM fibre was 2.6 times that of a SM, whereas this ratio for the mass (whole fibre) was only 1.8, indicating inferior properties in the core. Recently, Chen et al. [27] measured the electrical conductivity of carbon fibres whose radius was reduced by plasma-assisted etching. Based on a linear correlation between the tensile modulus and electrical conductivity of PAN-based carbon fibres, they were able to estimate the modulus of a fraction of the fibre (from 0.3 to 1.). We used their correlation factor and experimental data to estimate the modulus of reduced areas of carbon fibre. Figure 7 shows the variation of the elastic modulus [27, built from figure 3.f] of different PAN-based fibres (SM, IM, HM). The core of the fibre exhibits always a more compliant behaviour than that of the carbon fibre. Moreover, very different types of carbon fibres (from SM to HM) may have the same modulus for 0.3 times the initial radius and below 50 GPa. We have superimposed our results from Table 1 and found that our values are consistent with Fig. 7. Indeed, the modulus for HR40 is comparable to that of M40J, a HM carbon fibre close to HR40. As for the modulus of UTS50, it lies between two comparable SM fibres. Wang et al. [15] on 1-2 μm in diameter pillars, *i.e.* 3 to 6 times smaller (in radii than ours), found even lower values and this seems again rather consistent with Fig. 7. Let us note that the comparison between compressive and tensile moduli lies in the fact that these moduli are, for low strains, identical for a unidirectional ply, and therefore, by simple rule-of-mixtures, for the fibre [18, 28]. Therefore, the comparably low values of compressive moduli found

in this study compared to those of whole carbon fibres in tension, seem consistent and related to the differences in microstructure between the core of the fibre (our pillars) and its shell (or skin).

4.2. Mechanism of axial splitting and associated compressive strength

Our carbon fibre pillars fracture by axial splitting during micro-compression via the formation of cracks at or close to the contact surface between the top of the pillar and the flat punch indenter during the loading stage. Once the crack initiates it grows longitudinally with increasing compressive strain, then the fibres fail by axial splitting, with a classical failure mechanism for quasi brittle materials such as geo-materials, cements, concretes [29]. Similar behaviours during micro-compression tests were reported in some brittle or quasi-brittle materials in the literature. Semiconductors such as silicon (Si) [30], gallium arsenide (GaAs) [31], gallium nitride (GaN) [32], indium arsenide (InAs) [33] broke in similar way. Diamond has also been studied [34] and technical ceramics as well [33] such as MgO. Howie et al. [33] reported that the most common mode is through thickness axial splitting, in which the crack grows downward from intersecting slip bands in pillars above a critical size. The presence of slip bands is therefore attributed to some plasticity. These cracks initiate between the pillar and the indenter at the contact surface. The presence of some of these cracks has been attributed to the surface of the pillar being under a frictional constraint, as the pillar beneath deforms, and the surface being thrown into tension as the sample is unloaded. In our case thanks to the in situ imaging, we can rule out the unloading possibility. Cracks form during loading.

Hayes et al. [35], using a recoil test, observed some kink bands on their ultra-high modulus (UHM) pitch-based fibres. Oya and Johnson [4], using a compression device with a cantilever beam, observed some axial splitting at the contact (only images for UHM fibres - M60J - were presented), but it occurred after the onset of kink bands, which may be due to the bending produced by the cantilever loading. Nakatani et al. [3],

using a single fibre compression test, did not observe any kink bands nor Sugimoto et al. [36] (from SM to UHM PAN-based fibres). Tanaka et al. [8] did not address this issue nor Ueda and Akiyama [6]. Both were using single fibre compression tests.

During micro-compression tests, some experimental artefacts are likely to exist due to the small size of samples and their preparation. They include specimen taper, sample sinking into the substrate, friction at the interface between sample and indenter, and alignment of indenter and sample surfaces. We further look into them one after the other.

Due to constraints in the specimen fabrication, the taper in the micro-pillar cannot be avoided. The micro-pillar taper induces strain gradient during the deformation, and most of the deformation is confined to the top surface. At the beginning of the test, only the topmost portion of the sample deforms, since that portion is weak due to a smaller diameter, and it is more likely that it fails at the top where the indenter is in a contact. Due to taper, there will be non uniform stresses along the length of the micro-pillar. Our fabricated fibres UTS50 and HR40 have a taper angle of $\approx 2^{\circ}$. Howie et al. [33] investigated the effect of taper on compression of Silicon (Si) micropillars which has a taper angle of 2 and 4°. They found that the driving force for cracking mechanisms due to the taper is a secondary effect when axial crack nucleation is of importance.

In most of the FIB fabricated micro-pillars in the literature, the substrate has the same properties as micro-pillars. Due to compressive deformation, some amount of substrate deforms, where the micro-pillar sinks into the substrate. For our carbon fibres, we have used Sneddon's effect [22] to eliminate the substrate deformation. But, if the deformation is not homogeneous, we may overestimate the substrate deformation. The substrate deformation has an influence on the measurement of strain but not on the value of compressive strength.

The friction between the indenter and micropillar surface may have an influence on the deformation mechanisms. The friction between the indenter and the sample surface cannot be controlled due to small specimen size and it depends on the material. Howie

et al. [33] compared the axial splitting behaviour between Si, and magnesium oxide (MgO). MgO pillars exhibit top surface splitting, but not Si ones. In Si, the coefficient of friction between the indenter and the pillar was relatively low, 0.05, while for MgO, it was 0.17. Since friction is higher in the case of MgO, the pillar does not deform freely and it splits at the top surface. The friction prevents the pillar to deform freely causing a constraint at the contact surface, and this creates local stress concentrations and a multi-axial state of stress (see Supplementary B). Yet, the location of highest stress concentration is not at the contact surface. From the films (see supplemental) and Fig. 2, we know that the cracks nucleate in the upper part of the pillar. Still, we do not know whether this nucleation originates from the contact surface or below it.

Typically from micro-compression tests reported in literature, the specimen fails away from the contact surface (for metals, pillar yields at a slip plane where shear stress is maximum) of the micro-pillar but here the crack is initiating from the contact surface or close to it giving credit to the scenario of a stress concentration from an imperfect contact. As observed by Raabe et al. [37], the increased friction coefficient has a stabilising effect on the compression sample. When the pillar deforms, due to constraint at the top surface, tensile strains are induced allowing pillar to deform perpendicular to the axis which leads to axial splitting at the pillar surface. There is a possibility that the pillar slips away from the indenter when the friction is very low, which causes buckling in the micro-pillars. We did not see any buckling from our micro-compression tests. But friction may have some influence on fracture of the specimen at the contact surface which further leads to variation of compressive strength.

The possible improper alignment between the micro-pillar and the flat punch causes inhomogeneous deformation in the micro-pillar. With increasing compressive strain a small amount of misalignment can cause specimen to buckle or shear. For our samples, we did not see any buckling along the length of the micro-pillar.

The other possible artefact is due to sample preparation technique by FIB, where the sample preparation causes FIB-induced surface damage due to gallium ions. In com-

parison to the size of our micro-pillar, the damage is considered to be negligible. The thickness of gallium contents on the FIB machined Cu micro-pillars and beams was found to be $\approx$ 50 nm [38]. The advantage of testing FIB micropillar in comparison to single fibre compression tests [4] is that here we can control the diameter of the specimen. Sometimes, the carbon fibres are not circular due to their processing, but using FIB machining, we can get circular geometries, which will help in calculating the stress and strains accurately. From our results, we did not see any scattering in the stress-strain curves. Let us note also that axial splitting has been reported in the literature even for samples prepared without FIB-machining [4].

After reviewing the possible artefacts, we are prone to conclude that most of them have no influence on our compressive strength values except friction or imperfect local contact. The behaviour may not be the intrinsic response of carbon fibre pillars, and we might underestimate slightly the value of compression strength (see Supplemental B). It has been reported that in some PAN-based carbon fibres, a core-shell structure is likely to exist [26] so that a size effect may be at stake in our study. Albiez and Schwaiger [39] showed that for these diameters going from 6-7 μm (fibre diameters) to 3.5 μm (pillar diameter) the pillar size did note change the strength. Yet their carbon pillars were amorphous while our fibres have crystalline and amorphous parts, for which a possible size effect may occur. *Since our samples were FIB-machined, only the core structure is tested.*

4.3. Experimental method related compressive strength and possible skin/core effect

The lower strength in compression than in tension is observed by many authors. Table 3 shows the comparison of compression properties of our pillars and different PAN based carbon fibres or pillars reported in the literature from different experimental techniques. The ratio of compression strength to tensile strength for most of the fibres is usually less than one. We found however some contrasting results. The differences might be due either to the experimental method and methodology or from the nature of the

object tested in compression (the entire fibre or a part of it as a pillar as in this study). As for the former, Ueda and Akiyama [6] reported equivalent strengths in both tension and compression for T300 from single fibre micro-compression tests. The ratio compressive strength to tensile strength was 1.05 and the compressive strength 3.7 GPa. This latter value was linked to failure and not to an inflection point as for our definition (see § 3.3). In another study, for T300 carbon fibres, Oya and Johnson [4] reported compressive strength of 1.8 GPa, which is about 50% of its tensile strength. Their tests were not purely uniaxial compression tests, since load is applied with the use of cantilever beam bending with an end load. As for the latter liable explanation, as reported in Section 4.1, a strong skin-core structure may exist in the fibre so that the compressive strength of the core of the fibre might be very different from that of the whole fibre.

Additionally, Wang et al. [15] observed compressive strength values similar for SM and IM pillars (our results on SM and HM pillars are in agreement with that) and much lower for a UHM fibre. Ueda and Akiyama [6] had also similar values on SM and IM fibres. Oya and Johnson [4] found very different values (low) between SM and UHM fibres, with no clear correlation between tensile modulus and compressive strength (see Table 3). Shioya and Nakatani [40] also found low values on SM and HM fibres. Herráez et al. [16] found $\sim$ 3.5 GPa on a SM pillar. Therefore apart from Ref. [4, 40], recently reported values of compressive strengths are relatively similar, or at least, not as contrasted as the tensile strengths. We examine now the reasons that could explain these observations.

4.4. Understanding possible failure mechanisms

The mis-orientation angle of graphite crystallites with respect to the carbon fibre axis has an influence on the compressive strength. As observed by various authors [2, 3, 5, 25], generally the compressive strength increases with increase in the mis-orientation angle. Table 2 shows the mis-orientation angle of fibres having similar longitudinal tensile moduli than ours. The comparison is made with Ozcan et al. [41] data, where

authors determined the mis-orientation angle from X-ray diffraction measurement on PAN type fibres. We observe that there is no clear correlation.

Nakatani et al. [3] assumed that the compressive strength was limited by the buckling stress of individual carbon layers. They proposed a model where the buckling of crystallites is made easier by the presence of voids (unsupported regions). This estimation requires the measurement of structural parameters such as the interlayer spacing between graphene layers, the unsupported region (in terms of cross-section and aspect ratio) by WAXD and SAXS techniques. A similar estimation was made by Sugimoto et al. [5].

Tanaka et al. [8] also made such an assumption and proposed a closely related estimation (see Eq. (3)) for the compressive strength X_c^f:

$$X_c^f = \frac{\pi^2 \phi' E_0}{12} \left(\frac{d_{002}}{\alpha\, D} \right)^2 \tag{3}$$

where ϕ' is the ratio of the stress applied to the fibre against that experienced by the crystallites, estimated from mean field modelling [8] between 1.5 and 1.9. E_0 is the crystallite modulus (1.1 TPa), d_{002} is the interlayer spacing determined by XRD and αD is the transversely unsupported region, which is equivalent to the void length (α is the void aspect ratio and D is the void diameter). They compared their experimental values (see Table 3) with estimations based on Eq. (3) and measured structural parameters. They found estimated values to be one order of magnitude lower than their experimental values.

Recently, Okamoto and Ito [42] performed molecular dynamics simulations of PAN based carbon fibres containing both crystalline and amorphous structures. They showed that the amorphous part greatly affects the value for the compressive strength, and failure begins due to buckling of graphite crystallites but with increasing compressive strain the final failure happens due to shear slipping.

Tanaka et al. [8] proposed another interpretation of the failure mechanism. They

described the microstructure as containing crystalline carbon stacks surrounded by an amorphous carbon matrix. Mimicking the failure criterion of micro-buckling in continuous fibre composites proposed by Budiansky and Fleck [43] (see also [44, 45]), they assumed that the failure mechanism is linked to the progressive bending of carbon stacks oriented vis-a-vis the fibre direction and limited by the shear stiffness of the matrix (amorphous carbon). Eq. (4) describes this model.

$$X_c^f = \frac{G_{lt}^f}{1 + \frac{\bar{\phi}}{\gamma}} \tag{4}$$

where G_{lt}^f is the in-plane shear modulus of the fibre, γ is the shear yield strain and $\bar{\phi}$ the mis-orientation angle of the crystallites. Tanaka et al. [8] found a good correlation between estimations and experiments for a ratio $\frac{\bar{\phi}}{\gamma}$ of ~ 6.8.

We have plotted their estimation in Figure 8 for our pillars. For the shear modulus, we take the values determined by nano-indentation in our previous work [23] for UTS50 and HR40, a technique also employed by other authors [46, 47]. The indentations were made [23] at the centre of the fibre so that the parameters correspond to the pillars of the present work. We can observe that our results are very much in line with Tanaka et al. [8]'s model. We have added a trend line for $\frac{\bar{\phi}}{\gamma}$ of ~ 8 that describes adequately our results. Since there are some differences in the method of determination of the compressive strength (our method giving lower values), this new ratio seems relevant.

It is observed that UTS50 and HR40 have similar shear [23] and compressive (see Table 1) moduli in their cores. This might indicate that similar crystalline orientations $\bar{\phi}$ exist in the core of both fibres. This will, in turn, gives similar compressive strengths of the cores of fibres following Tanaka et al. [8]. Our experimental results are therefore in agreement with the nano-buckling estimation of Tanaka et al. [8].

5. Concluding remarks

In-situ SEM micro-compression tests were carried out on FIB-machined carbon fibre micro-pillar samples under quasi-static or cyclic conditions. The tests were performed on two different PAN-based fibres with different longitudinal tensile moduli. The failure mechanism is an axial crack that occurs at or near the contact surface between the flat punch indenter and the pillar. The mechanical response of the test, the force-displacement curve, after a fully elastic linear regime, shows an inflection point associated with the onset of cracking observed by SEM, defined as pseudo-yielding. In cyclic tests, large hysteretic loops can be observed after the onset of cracking, which are completely reversible, i.e. without any plasticity. The compressive strength values, defined at the inflection point, are found to be lower than tensile strength values for carbon fibres. The compressive moduli are also found to be much lower than tensile moduli values for carbon fibres. The existence of a core/shell structure is discussed. The properties extracted from this study on pillars machined from fibres are related to the core structure of carbon fibres. This results in lower properties as compared to the whole fibre and similar values for SM and HM carbon fibres.

The different mechanisms reported in literature for modelling the compressive failure of carbon fibres are reviewed and compared to our experimental values. The scenario of nano-buckling of crystalline carbon stacks constrained by the shear stiffness of the fibre is found to be in agreement with our results.

Acknowledgements

Région Bretagne and Univ. Bretagne Loire (project INDFIBRE) are acknowledged for financial support.

Data availibility

The raw/processed data can be found in the Supplemental D.

References

[1] Jones, W.R., Johnson, J.W.. Intrinsic strength and non-hookean behaviour of carbon fibres. Carbon N Y 1971;9(5):645–655.

[2] Dobb, M.G., Johnson, D.J., Park, C.R.. Compressive strengths of single carbon fibres and composite strands. J Mater Sci 1990;25(2):829–834.

[3] Nakatani, M., Shioya, M., Yamashita, J.. Axial compressive fracture of carbon fibers. Carbon N Y 1999;37(4):601–608.

[4] Oya, N., Johnson, D.J.. Longitudinal compressive behaviour and microstructure of PAN-based carbon fibres. Carbon N Y 2001;39(5):635–645.

[5] Sugimoto, Y., Kato, T., Shioya, M., Kobayashi, T., Sumiya, K., Fujie, M.. Structure change of carbon fibers during axial compression. Carbon N Y 2013;57:416–424.

[6] Ueda, M., Akiyama, M.. Compression test of a single carbon fiber in a scanning electron microscope and its evaluation via finite element analysis. Adv Compos Mater 2019;28(1):57–71.

[7] Loidl, D., Paris, O., Burghammer, M., Riekel, C., Peterlik, H.. Direct Observation of Nanocrystallite Buckling in Carbon Fibers under Bending Load. Phys Rev Lett 2005;95(22):225501.

[8] Tanaka, F., Okabe, T., Okuda, H., Kinloch, I.A., Young, R.J.. The effect of nanostructure upon the compressive strength of carbon fibres. J Mater Sci 2013;48(5):2104–2110.

[9] Newcomb, B.A.. Processing, structure, and properties of carbon fibers. Compos Part A Appl Sci Manuf 2016;91:262–282.

[10] Kiener, D., Motz, C., Dehm, G.. Dislocation-induced crystal rotations in micro-compressed single crystal copper columns. J Mater Sci 2008;43:2503–2506.

[11] Guruprasad, T.S., Bhattacharya, S., Basu, S.. Size effect in microcompression of polystyrene micropillars. Polymer (Guildf) 2016;98:118–128.

[12] Kermouche, G., Guillonneau, G., Michler, J., Teisseire, J., Barthel, E.. Perfectly plastic flow in silica glass. Acta Mater 2016;114:146–153.

[13] Mayer, C.R., Molina-Aladareguia, J., Chawla, N.. Three dimensional (3D) microstructure-based finite element modeling of Al-SiC nanolaminates using focused ion beam (FIB) tomography. Mater Charact 2016;120:369–376.

[14] Singh, S., Kaira, C.S., Bale, H., Huynh, C., Merkle, A., Chawla, N.. In situ micropillar compression of Al/SiC nanolaminates using laboratory-based nanoscale X-ray microscopy: Effect of nanopores on mechanical behavior. Mater Charact 2019;150:207–212.

[15] Wang, J., Salim, N., Fox, B., Stanford, N.. Anisotropic compressive behaviour of turbostratic graphite in carbon fibre. Appl Mater Today 2017;9:196–203.

[16] Herráez, M., Bergan, A.C., Lopes, C.S., González, C.. Computational micromechanics

model for the analysis of fiber kinking in unidirectional fiber-reinforced polymers. Mech Mater 2020;142:103299.

[17] Nunna, S., Ravindran, A.R., Mroszczok, J., Creighton, C., Varley, R.J.. A review of the structural factors which control compression in carbon fibres and their composites. Composite Structures 2023;303:116293.

[18] Keryvin, V., Marchandise, A., Mechin, P.Y., Grandidier, J.C.. Determination of the longitudinal non linear elastic behaviour and compressive strength of a CFRP ply by bending tests on laminates. Compos Part B Eng 2020;187:107863.

[19] Mechin, P.Y., Keryvin, V., Grandidier, J.C.. Limitations on adding nano-fillers to increase the compressive strength of continuous fibre / epoxy matrix composites. Compos Sci Technol 2020;192:108099.

[20] Toho Tenax. http://www.asprotec.ru/pub/UTS50.pdf; 2012.

[21] Mitsubishi Chemical. https://www.m-chemical.co.jp/en/products/departments/mcc/cfcm/product/CFtow_Jan2020en.pdf; 2020.

[22] Sneddon, I.N.. The relation between load and penetration in the axisymmetric boussinesq problem for a punch of arbitrary profile. Int J Eng Sci 1965;3(1):47–57.

[23] Guruprasad, T., Keryvin, V., Charleux, L., Guin, J.P., Arnould, O.. On the determination of the elastic constants of carbon fibres by nanoindentation tests. Carbon N Y 2021;173:572–586.

[24] Prasad, K.E., Keryvin, V., Ramamurty, U.. Pressure sensitive flow and constraint factor in amorphous materials below glass transition. J Mater Res 2009;24(3):890–897.

[25] Paris, O., Peterlik, H.. Single Carbon Fibres: Structure from X-ray Diffraction and Nanomechanical Properties. Vienna: Springer Vienna. ISBN 978-3-7091-1887-0; 2016, p. 1–28.

[26] Kobayashi, T., Sumiya, K., Fukuba, Y., Fujie, M., Takahagi, T., Tashiro, K.. Structural heterogeneity and stress distribution in carbon fiber monofilament as revealed by synchrotron micro-beam x-ray scattering and micro-raman spectral measurements. Carbon 2011;49(5):1646–1652.

[27] Chen, L., Hao, L., Liu, S., Ding, G., Sun, X., Zhang, W., et al. Modulus distribution in polyacrylonitrile-based carbon fiber monofilaments. Carbon 2020;157:47–54.

[28] Keryvin, V., Marchandise, A., Grandidier, J.C.. Non-linear elastic longitudinal behaviour of continuous carbon fibres/epoxy matrix composite laminae: Material or geometrical feature? Composites Part B: Engineering 2022;247:110329.

[29] Ashby, M., Sammis, C.. The damage mechanics of brittle solids in compression. Pure Appl Geophys 1990;133(3):489–521.

[30] Östlund, F., Rzepiejewska-Malyska, K., Leifer, K., Hale, L.M., Tang, Y., Ballarini, R., et al. Brittle-to-Ductile Transition in Uniaxial Compression of Silicon Pillars at Room Temperature. Adv

Funct Mater 2009;19(15):2439–2444.

[31] Östlund, F., Howie, P., Ghisleni, R., Korte-Kerzel, S., Leifer, K., Clegg, W.B., et al. Ductile-brittle transition in micropillar compression of GaAs at room temperature. Philos Mag 2011;91:1190–1199.

[32] Fan, S., Li, X., Fan, R., Lu, Y.. Size-dependent fracture behavior of GaN pillars under room temperature compression. Nanoscale 2020;12(45):23241–23247.

[33] Howie, P.R., Korte, S., Clegg, W.J.. Fracture modes in micropillar compression of brittle crystals. J Mater Res 2012;27(1):141–151.

[34] Wheeler, J., Raghavan, R., Wehrs, J., Zhang, Y., Erni, R., Michler, J.. Approaching the Limits of Strength: Measuring the Uniaxial Compressive Strength of Diamond at Small Scales. Nano Lett 2015;16.

[35] Hayes, G.J., Edie, D.D., Kennedy, J.M.. The recoil compressive strength of pitch-based carbon fibres. J Mater Sci 1993;28(12):3247–3257.

[36] Sugimoto, Y., Shioya, M., Yamamoto, K., Sakurai, S.. Relationship between axial compression strength and longitudinal microvoid size for PAN-based carbon fibers. Carbon N Y 2012;50(8):2860–2869.

[37] Raabe, D., Ma, D., Roters, F.. Effects of initial orientation, sample geometry and friction on anisotropy and crystallographic orientation changes in single crystal microcompression deformation: A crystal plasticity finite element study. Acta Mater 2007;55(13):4567–4583.

[38] Kiener, D., Motz, C., Rester, M., Jenko, M., Dehm, G.. {FIB} damage of Cu and possible consequences for miniaturized mechanical tests. Mater Sci Eng A 2007;459(1):262–272.

[39] Albiez, A., Schwaiger, R.. Size Effect on the Strength and Deformation Behavior of Glassy Carbon Nanopillars. MRS Advances 2019;4:133–138.

[40] Shioya, M., Nakatani, M.. Compressive strengths of single carbon fibres and composite strands. Compos Sci Technol 2000;60(2):219–229.

[41] Ozcan, S., Vautard, F., Naskar, A.K.. Designing the Structure of Carbon Fibers for Optimal Mechanical Properties; chap. 10. 2014, p. 215–232.

[42] Okamoto, S., Ito, A.. Molecular Dynamics Analysis on Compressive Strength of PAN-Based Carbon Fibers. Int J Nanosci 2014;13:1440004.

[43] Budiansky, B., Fleck, N.. Compressive failure of fibre composites. J Mech Phys Solids 1993;41(1):183–211.

[44] Mechin, P.Y., Keryvin, V., Grandidier, J.C., Glehen, D.. An experimental protocol to measure the parameters affecting the compressive strength of CFRP with a fibre micro-buckling failure criterion. Compos Struct 2019;211:154–162.

[45] Mechin, P.Y., Keryvin, V., Grandidier, J.C.. Effect of the nano-filler content on the compressive

strength of continuous carbon fibre/epoxy matrix composites. Compos Part B Eng 2021;224:109223.

[46] Shirasu, K., Goto, K., Naito, K.. Microstructure-elastic property relationships in carbon fibers: A nanoindentation study. Compos Part B Eng 2020;200:108342.

[47] Csanádi, T., Németh, D., Zhang, C., Dusza, J.. Nanoindentation derived elastic constants of carbon fibres and their nanostructural based predictions. Carbon N Y 2017;119:314–325.

Table 1 Compression modulus (E_c^p) of carbon fibres (with tensile modulus E_t^f) micropillars

Fibre name	E_t^f [GPa]	E_c^p [GPa]
UTS50	240	121 $\pm$6
HR40	375	95 $\pm$ 12

Table 2 Comparison of tensile modulus, tensile strength of fibres (from suppliers datasheets), compressive strength of pillars (from this work, superscript 'p') and mis-orientation angle (ϕ) of similar PAN-based fibres (from Ozcan et al. [41]).

Fibre name (This work)	E_t^f [GPa]	X_t^f [GPa]	X_c^p [GPa]	X_c^p/X_t^f Ratio [-]	Fibre name [41]	Misorientation angle ϕ [°] [41]	L_c [nm] [41]	Void size [nm] [41]
UTS50	240	4.8	2.38$\pm$ 0.1	0.50$\pm$0.02	T700	16.8	1.8	9.05
HR40	375	4.4	2.36$\pm$ 0.4	0.54$\pm$0.09	UHMS	9.9	4.8	10.5

Table 3 Comparison of determined compressive strength of fibres (X_c^f) or pillars (X_c^p) with literature for different PAN based carbon fibres. The values for tensile elastic modulus (E_t^f), tensile strength (X_t^f), and ratio of compression strength to tensile strength are also added. All the values are in GPa.

Carbon fibre name	E_t^f	$X_c^{f,p}$	X_t^f	$X_c^{f,p}/X_t^f$	Reference
HT00	214	-	-	0.89	Loidl et al. [7]
HT18	256	-	-	0.65	X_c^f calculated theoretically assuming
HT21	320	-	-	0.51	only crystalline part
HT24	378	-	-	0.52	(Two point bending tests)
T300	210	1.8	3.5	0.51	
T700S	237	2.4	5.3	0.45	
T800H	306	2.3	6.4	0.36	Oya and Johnson [4]
T1000	294	2.8	7.1	0.39	X_c^f=Ultimate failure strength
M40J	335	1.8	4.9	0.37	(Not a pure compression test)
M50J	430	1.3	4.3	0.30	
M60J	535	1.0	3.5	0.29	
T300	230	3.71	3.53	1.05	Ueda and Akiyama [6]
					X_c^f=Ultimate failure strength
T800S	294	3.69	5.88	0.63	(Single fibre compression test)
H4	235	2.015	4.9	0.41	Shioya and Nakatani [40]
T4	395	1.61	4.42	0.36	(Single fibre compression test)
M46J	436	1.69	4.2	0.40	Wang et al. [15]
IM7	276	2.97	5.5	0.54	X_c^p=Ultimate failure strength
SM (in-house)	203	3.03	2.8	1.08	(FIB, micro-compression tests)
					Herráez et al. [16]
AS4	230	3.5	4	0.88	X_c^p at 2% displacement offset
					(FIB, micro-compression tests)
UTS50	240	2.38	4.80	0.50	This work
HR40	375	2.36	4.41	0.54	X_c^p at $\approx 1\%$ strain offset
					(FIB, micro-compression tests)

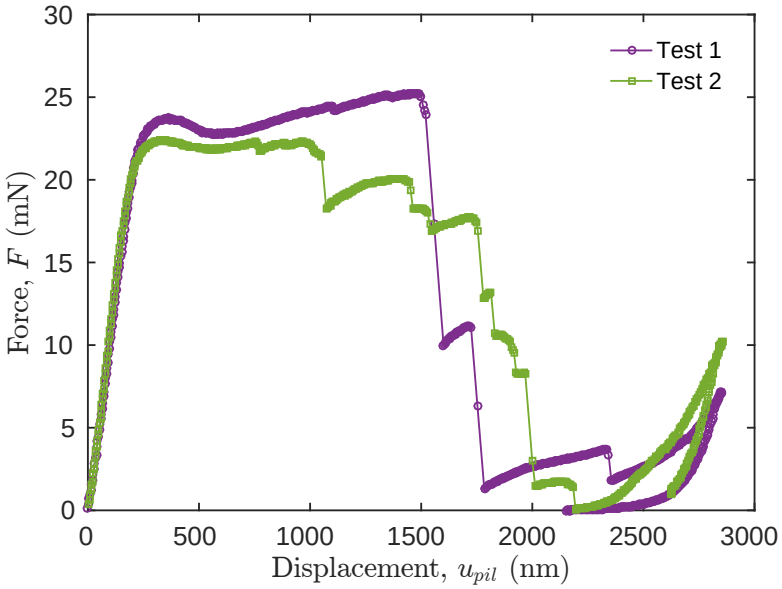

Fig. 1. Load displacement curves of UTS50 carbon fibre micro pillars in compression.

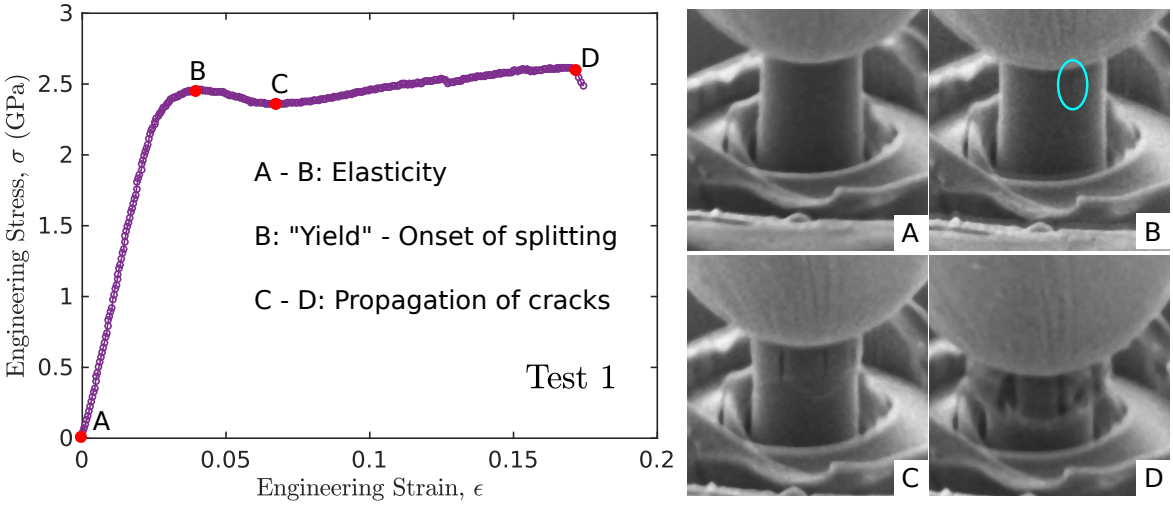

Fig. 2. Engineering stress-strain response of UTS50 micro-pillar in compression, and SEM images of deformed micro-pillar at different stages of compressive strain. The SEM images A,B,C, and D corresponds to points on the curve, and the elliptic mark shows the axial splitting at the inflection point. The pillar diameter is 3.5 µm.

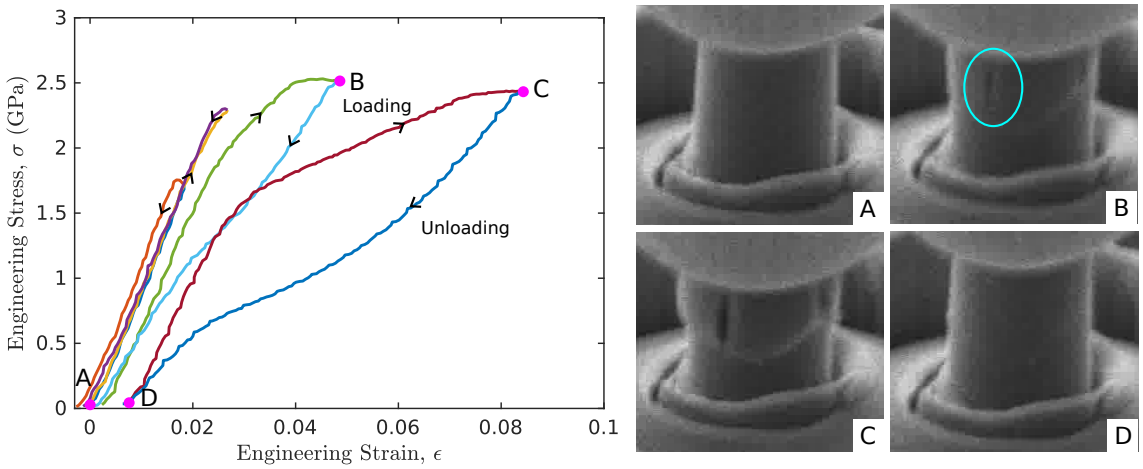

Fig. 3. Engineering stress-strain response of UTS50 micro-pillar in compression due to cyclic loading, and SEM images of deformed micro-pillar at different stages of compressive strain. The SEM images A, B, C, and D correspond to points on the curve, and the elliptic mark shows the axial splitting. The pillar diameter is 3.5 µm.

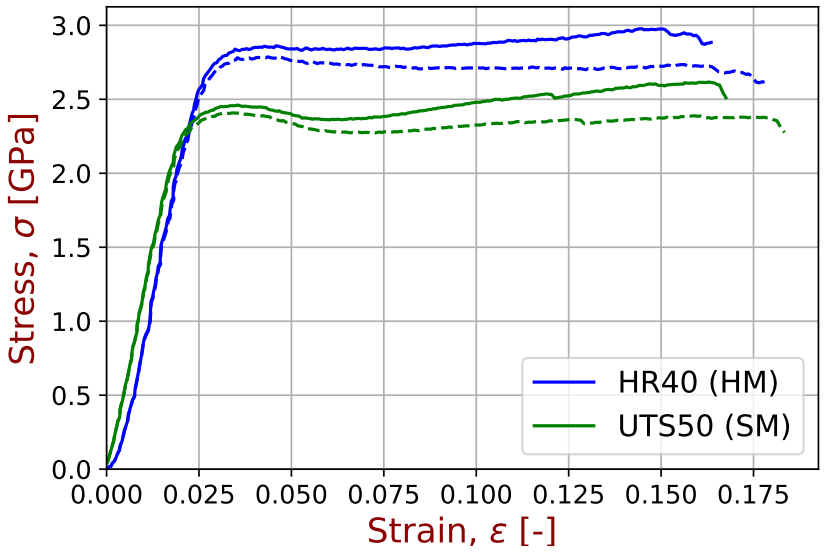

Fig. 4. Stress strain response in compression of micro-pillars of carbon fibres UTS50 and HR40: engineering curves (–) or true stress-true strain curves (- -).

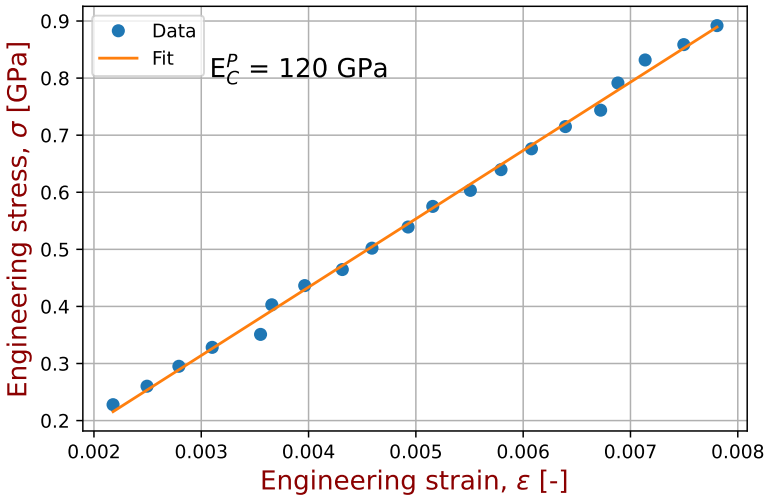

Fig. 5. Determination of a compressive elastic modulus. Example for UTS50 carbon fibre micropillar.

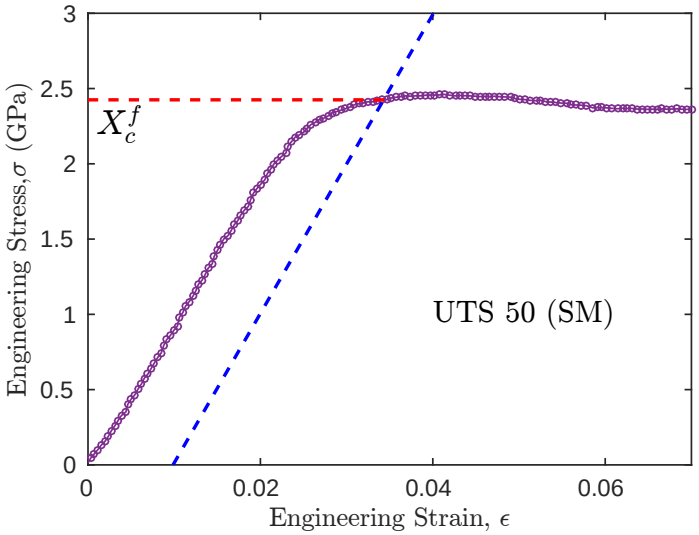

Fig. 6. A schematic of the method for determining the inflection point from Engineering Stress strain curves (UTS50). The inclined vertical line is a 1% linear strain offset, and the horizontal line is drawn from the inflection point, which is the intersection of offset line and curves.

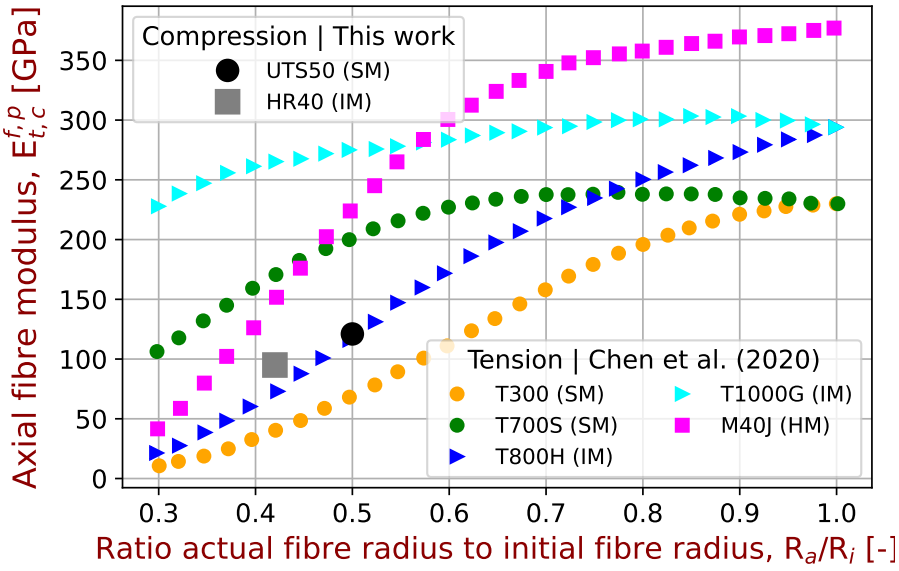

Fig. 7. Evolution of the tensile modulus of carbon fibres (E_t^f) of initial radius R_i (fibre) and actual radius R_a (etched fibre) for different types of carbon fibres (plot built from [27]). The moduli obtained by microcompression tests on carbon fibre pillar (E_c^p) from the present study are superimposed.

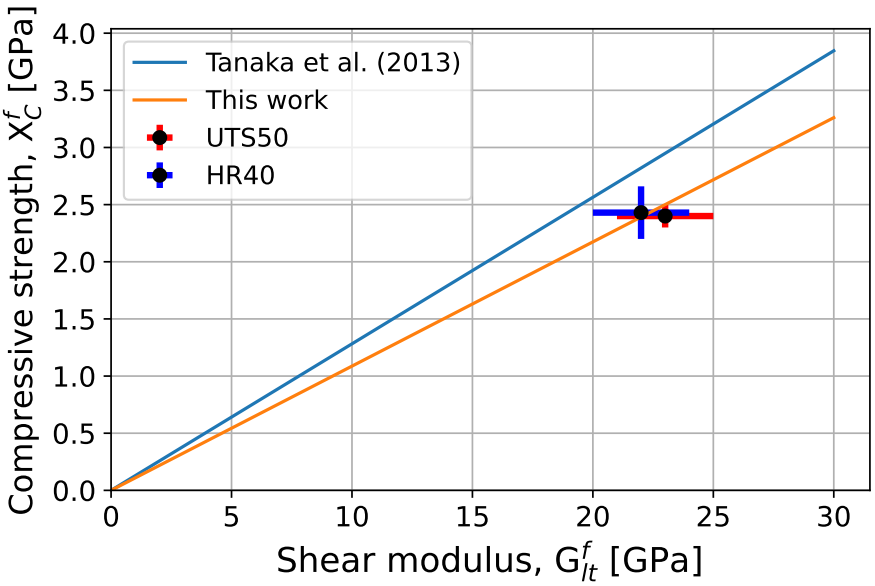

Fig. 8. Plot of measured fibre compressive strength versus the fibre shear modulus